Available online at www.sciencedirect.com
SCIENCE DIRECT®
Comput. Methods Appl. Mech. Engrg. 193 (2004) 3195–3220
Computer methods in applied mechanics and engineering
www.elsevier.com/locate/cma

Continuum approach to material failure in strong discontinuity settings

J. Oliver *, A.E. Huespe [1]

E.T.S. Enginyers de Camins, Canals i Ports, Technical University of Catalonia (UPC), Módul C-1, Gran Capitan s/n, Campus Nord UPC, Jordi Girona 3, 08034 Barcelona, Spain

Received 8 January 2003; received in revised form 22 July 2003; accepted 23 July 2003

Abstract

The paper focuses the numerical modelling of material failure in a strong discontinuity setting using a continuum format. Displacement discontinuities, like fractures, cracks, slip lines, etc., are modelled in a strong discontinuity approach, enriched by a transition from weak to strong discontinuities to get an appropriate representation of the fracture process zone. The introduction of the strong discontinuity kinematics automatically projects any standard dissipative constitutive model, equipped with strain softening, into a discrete traction–separation law that is fulfilled at the discontinuity interface. Numerical issues like a global discontinuity tracking algorithm via a heat conduction-like problem are also presented. Some representative numerical simulations illustrate the performance of the presented approach.

Keywords: Material failure; Fracture; Localization; Strong discontinuities; Traction–separation law

1. Introduction

Computational failure mechanics can be understood as the set of mathematical and computational tools aiming at: (a) identifying the mechanisms of the structural failure, (b) quantifying the corresponding critical actions and (c) modelling the post-critical behaviour of the structures. In a fairly general setting one could commonly identify two different types of failure:

- *Geometrical failure*. Connected to the global geometrically non-linear behaviour of the structure leading to critical (unstable) spatial configurations.
- *Material failure*. Associated to a local specific behaviour of the material points entailing the progressive softening of the material response that spreads across the body and leads to the structural failure.

* Corresponding author. Fax: +34-93-401-1048.
E-mail address: oliver@cimne.upc.es (J. Oliver).
[1] Cime-Conicet, Argentina. Present address: E.T.S. Enginyers de Camins Canals i Ports, UPC, Barcelona, Spain.

0045-7825/$ - see front matter
doi:10.1016/j.cma.2003.07.013

Traditionally, both types of failure have been treated in a quite separate manner and through different mathematical tools. Geometrical failure has been tackled from a *continuum* point of view through well developed tools that include ingredients of non-linear kinematics and (in general) linear elastic or strain-hardening constitutive equations. On the other hand, material failure has been many times associated to the onset and development of material discontinuities which, depending on the context, have been termed cracks, slip-lines, fractures, localization bands, etc. Linear fracture mechanics can be considered a precursor tool and then, two different branches emerged:

(a) non-linear *discrete* fracture mechanics [11], based on modelling discrete cohesive surfaces, that are ruled by specific traction–separation laws, independent from the constitutive behaviour at the bulk of the material, whose local softening and propagation leads to the structural failure, and
(b) *continuum* approaches based on the classical continuum (strain localization [16], smeared cracking [26]) or the enriched continuum (gradient enrichment, Cosserat continuum, non-local models [7]) that aim at modelling the concentration of the strains in narrow bands, via the introduction of constitutive strain softening [32], whose propagation makes eventually the structure to fail.

More recently a third way has emerged from the introduction of the *strong discontinuity* concept [1,17,28,29] that, although not always has been exploited in this sense, allows one to bridge both continuum and discrete approaches to material failure. In fact it can be shown [19], that *the introduction of strong discontinuity kinematics in a continuum medium*, ruled by continuum (stress–strain) constitutive equations equipped with strain softening, *induces the fulfillment of specific traction–separation constitutive laws at a discrete set of propagating cohesive surfaces*. This bridge can then be exploited for different purposes, namely:

- To keep the failure analysis in a continuum format for both geometrical and material failure. In consequence, simultaneous combination of both types of failure, that can become relevant for some structural types like slender structures, becomes natural and easier.
- As a tool for identification of material properties and constitutive laws to model fracture and material failure from laboratory tests. In fact, in many cases laboratory mechanical tests provide *spatially averaged* results, in terms of local forces or local displacements, that do not discriminate continuum from discontinuum and, therefore, do not provide direct information about traction–separation laws which have to be assessed by some "ad hoc" interpretation of the results. In that sense a continuum constitutive behaviour can be more easily drawn from laboratory tests. Then, though not necessarily, from those continuum models the inherited discrete traction–separation laws can be analytically derived.
- The aforementioned connection with non-linear fracture mechanics allows one to take advantage of the very well known set of material properties and parameters used in non-linear fracture mechanics to characterize material behaviour. A paradigm of this is the fracture energy concept that can be shown to play a similar role in continuum and discrete approaches to characterize the material softening.

This paper is devoted to describe the analytical and computational ingredients of a *continuum strong discontinuity approach* (CSDA) *to material failure* that plays that role of bridging continuum and discrete failure mechanics [21]. After examining the physical problem to model in Section 2, a strong discontinuity scenario is introduced in Section 3 where the effects of strong discontinuum kinematics into continuum constitutive models are examined. Then, in Section 4, some numerical aspects like finite elements with embedded discontinuities and discontinuity tracking algorithms are explored. Finally, in Section 5 representative numerical simulations are undertaken.

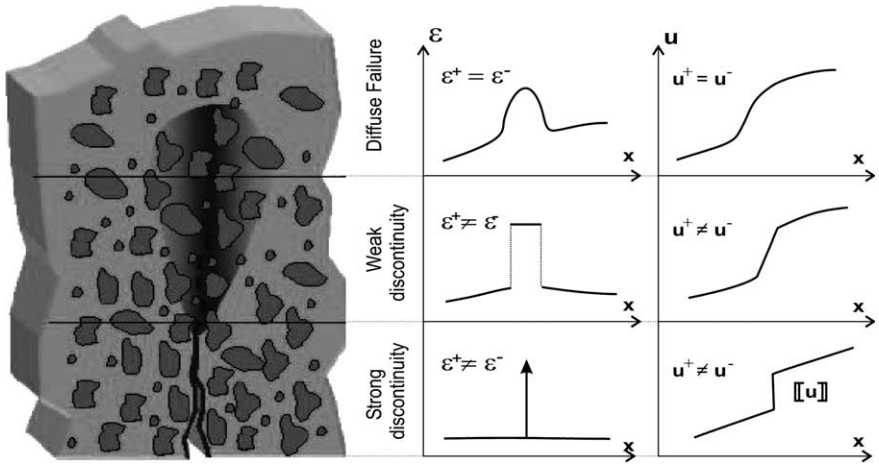

Fig. 1. Fracture process.

2. Motivation: The fracture process

It is commonly accepted that, for quasibrittle geomaterials, fracture takes place through a transition process, involving formation and coalescence of micro cracks [3,12], that takes a given material point from a continuum macroscopical status to a discontinuum one. Also for ductile metallic materials, fracture is understood as voids nucleation and coalescence, that eventually collapses into a macroscopical discontinuity. This facts can be translated into the spatial locus of points, for different stages of the fracture process, sketched in Fig. 1. There, three different zones can be distinguished:

- *Diffuse failure zone*. It is characterized by the initiation of the dissipation phenomena resulting into an increase and concentration of the strains. However this fact does not translate yet into the appearance of material discontinuities and both the strains and the stresses are spatially smooth.
- *Weak discontinuity zone*. The previous zone becomes narrower and the concentration of the strains sharper up to collapse (localize) into a discontinuous strain field [2] $\boldsymbol{\varepsilon}$. The displacement field, however, remains continuous. This scenario, exhibiting discontinuous strains and continuous displacements, will be from now on termed *weak discontinuity*.
- *Strong discontinuity zone*. The weak discontinuity develops into a band whose size is getting narrower and narrower up to collapse into a zero thickness discontinuity band. The displacement field experiences a real jump $[\![\mathbf{u}]\!]$ and any strain measure involving spatial gradients of the displacements becomes unbounded.

The three zones above constitute what in classical fracture mechanics is termed the Fracture Process Zone ([2]). The capture of the dissipation phenomena taking place at each of them is one of the goals of the CSDA. [3]

[2] In the context of continuum approaches this is commonly termed *strain localization*.
[3] This motivates the kinematics considered in Section 3.1.

2.1. Continuum failure models: non-linear strain softening models

Let us consider the class of non-linear, rate independent, dissipative constitutive models described by the following ingredients:

$$\text{Free energy:} \quad \Psi((\boldsymbol{\varepsilon}-\boldsymbol{\varepsilon}^{(i)}),q), \tag{1a}$$

$$\text{Constitutive equations:} \quad \begin{cases} \boldsymbol{\sigma} = \partial_{\varepsilon}\Psi((\boldsymbol{\varepsilon}-\boldsymbol{\varepsilon}^{(i)}),q) = -\partial_{\varepsilon^{(i)}}\Psi((\boldsymbol{\varepsilon}-\boldsymbol{\varepsilon}^{(i)}),q), \\ \alpha = \partial_{q}\Psi((\boldsymbol{\varepsilon}-\boldsymbol{\varepsilon}^{(i)}),q), \end{cases} \tag{1b,c}$$

$$\text{Internal variable evolution:} \quad \begin{cases} \dot{\boldsymbol{\varepsilon}}^{(i)} = \lambda \mathbf{m}(\sigma), \\ \dot{\alpha} = \lambda, \end{cases} \tag{1d,e}$$

$$\text{Yield/damage function:} \quad f(\boldsymbol{\sigma},q) \equiv \phi(\boldsymbol{\sigma}) - q, \tag{1f}$$

$$\text{Softening law:} \quad \dot{q} = H(q)\dot{\alpha}; \quad H<0; \quad q\in[0,\sigma_u] \begin{cases} q|_{t=0} = \sigma_u, \\ q|_{t=\infty} = 0, \end{cases} \tag{1g}$$

$$\text{Loding/unloading conditions:} \quad \lambda \geqslant 0 \quad f \leqslant 0 \quad \lambda f = 0, \tag{1h}$$

$$\text{Persistency condition:} \quad \lambda \dot{f} = 0 \quad \text{iff} \quad f = 0, \tag{1i}$$

$$\text{Dissipation density:} \quad \mathscr{D} = \boldsymbol{\sigma} : \dot{\boldsymbol{\varepsilon}} - \dot{\Psi} = \boldsymbol{\sigma} : \dot{\boldsymbol{\varepsilon}}^{(i)} - \alpha\dot{q} \geqslant 0, \tag{1j}$$

where Ψ is the density of Helmholz's free energy, $\boldsymbol{\varepsilon}(\mathbf{x},t)$ and $\boldsymbol{\sigma}(\mathbf{x},t)$ stand for the strains and stresses, respectively, $\boldsymbol{\varepsilon}^{(i)}$ are the inelastic (internal variables) strains, q is the stress-like variable and α the strain-like internal variable (thermodynamically conjugate of q according to Eq. (1c)), λ is the plastic/damage multiplier and $\mathbf{m}(\boldsymbol{\sigma})$ the inelastic flow-tensor. In (1f) $\phi(\boldsymbol{\sigma})$ is the uniaxial equivalent stress (an homogeneous function of degree one of the stresses) and $f(\boldsymbol{\sigma},q)$ the yield/damage function defining the elastic domain $\mathsf{E}_{\sigma} := \{\sigma; f(\sigma,q) \equiv \phi(\boldsymbol{\sigma}) - q < 0\}$ whose size is determined by the softening variable q, that evolves according to the softening law (1g)), in terms of the continuum softening modulus $H<0$. Finally Eqs. (1h)–(1j) are the classical equations defining the loading/unloading conditions and Eq. (1j) states the positive character of the volumic dissipation $\mathscr{D}$.

One can easily identify in the setting provided by Eq. (1) different families of continuum constitutive equations frequently used to model continuum failure. In particular, elasto-plastic models [14,30] and isotropic damage [31] models are obtained from the following specifications:

$$\text{Elasto-plastic models:} \quad \boldsymbol{\varepsilon}^{(i)} = \boldsymbol{\varepsilon}^{p}; \quad \Psi((\boldsymbol{\varepsilon}-\boldsymbol{\varepsilon}^{p}),q) \equiv \tfrac{1}{2}(\boldsymbol{\varepsilon}-\boldsymbol{\varepsilon}^{p}) : \mathbf{C} : (\boldsymbol{\varepsilon}-\boldsymbol{\varepsilon}^{p}) + \mathsf{H}^{-1}(q), \tag{2a}$$

$$\text{Isotropic damaged models:} \quad \boldsymbol{\varepsilon}^{(i)} = \mathbf{0}; \quad \Psi(\boldsymbol{\varepsilon},q) \equiv \tfrac{1}{2}[1-d(q)] \quad \boldsymbol{\varepsilon} : \mathbf{C} : \boldsymbol{\varepsilon}, \tag{2b}$$

where $\boldsymbol{\varepsilon}^{\mathrm{p}}$ stands for the plastic strains, $d(q)$ $(0 \leqslant d \leqslant 1)$ is the damage variable and $\mathbf{C} = \hat{\lambda}\mathbf{1}\otimes\mathbf{1} + 2\boldsymbol{\mu}\mathbf{I}$ is the fourth-order elasticity tensor ($\mathbf{1}$ and $\mathbf{I}$ being, respectively, the second- and fourth-order unit tensors and $\hat{\lambda}$ and μ the Lame's constants). In Eq. (2a) $\mathsf{H}^{-1}(q)$ is the plastic potential providing the internal variable $\alpha = \partial_q \mathsf{H}^{-1}(q)$ through Eq. (1c) and the softening modulus from Eq. (1g) as $H^{-1} = \partial_q \mathsf{H}^{-1}(q)$.

3. A strong discontinuity setting

Strong discontinuities are understood here as jumps in the displacement field experienced by solids during deformation processes. Therefore, cracks (in concrete), fractures (in rocks) slip lines (in soils) and

shear bands (in metals) are all them different types of strong discontinuities. In this setting we will accommodate these discontinuities in a Continuum Mechanics format (despite the semantic contradiction of both words) in such a way that existing analytical results and computational methods developed for continuum material failure can be immediately extended to discontinuous solids. In the following sections the main elements of this setting are presented.

3.1. Strong discontinuity kinematics: weak/strong discontinuities

Let us consider a body Ω experiencing a strong discontinuity along a material surface S, that splits the body into two parts Ω^+ and Ω^- such that the normal $\mathbf{n}$ to S points to Ω^+ (see Fig. 2). The rate of displacement field can be mathematically described as

$$\dot{\mathbf{u}}(\mathbf{x},t) = \dot{\bar{\mathbf{u}}}(\mathbf{x},t) + H_S[\![\dot{\mathbf{u}}]\!](\mathbf{x},t), \tag{3}$$

where H_S stands for the Heaviside (step) function ($H_S(\mathbf{x}) = 1\ \forall \mathbf{x} \in \Omega^+$ and $H_S(\mathbf{x}) = 0\ \forall \mathbf{x} \in \Omega^-$) and $\dot{\bar{\mathbf{u}}}(\mathbf{x},t) : \Omega \times [0,T] \to R^{n_{\dim}}$ and $[\![\dot{\mathbf{u}}]\!](\mathbf{x},t) : \Omega \times [0,T] \to R^{n_{\dim}}$ are continuous functions ($n_{\dim}$ and $([0,T])$ being, respectively, the dimension of the problem and the time interval of interest). Then, the continuum rate of strains field *compatible* with the displacements (3) can be written as (see Fig. 2)

$$\text{Strong discontinuity kinematics:} \quad \begin{cases} \dot{\boldsymbol{\varepsilon}}(\mathbf{x},t) = \nabla^{\mathrm{s}}\dot{\mathbf{u}} = \underbrace{\dot{\bar{\boldsymbol{\varepsilon}}}(\mathbf{x},t)}_{\text{regular (bounded)}} + \underbrace{\delta_S([\![\dot{\mathbf{u}}]\!] \otimes \mathbf{n})^S}_{\text{singular (unbounded)}}, \\ [\![\dot{\mathbf{u}}]\!] = \dot{\mathbf{u}}|_{\mathbf{X}\in\Omega^+\cap S} - \dot{\mathbf{u}}|_{\mathbf{x}\in\Omega^-\cap S}, \end{cases} \tag{4}$$

where ∇^{s} stands for the symmetric gradient operator and δ_S is the Dirac's delta function placed at S ($\nabla H_S = \delta_S \mathbf{n}$ in the distributional sense). Observe, in Eq. (4) and Fig. 2, the unbounded character of the strain field at the discontinuity interface S, which constitutes the most relevant feature of the strong discontinuity kinematics. For the subsequent mathematical analysis it is convenient to consider a regularized version of the kinematics in Eq. (4) by defining a discontinuity band S^h (of bandwidth h) containing the discontinuity surface S (see Fig. 3) and approaching the Dirac's delta function δ_S by a sequence of h-regularized Dirac's delta functions, δ_S^h, defined as

$$\delta_S = \lim_{h\to 0} \delta_S^h(\mathbf{x}), \quad \delta_S^h(\mathbf{x}) = \frac{1}{h}\mu_S^h(\mathbf{x}), \quad \mu_S^h(\mathbf{x}) = \begin{cases} 1 & \forall \mathbf{x} \in S^h, \\ 0 & \forall \mathbf{x} \in \Omega \setminus S^h, \end{cases} \tag{5}$$

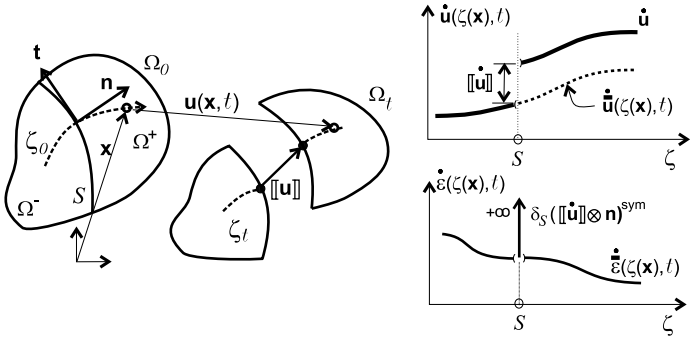

Fig. 2. Strong discontinuity kinematics.

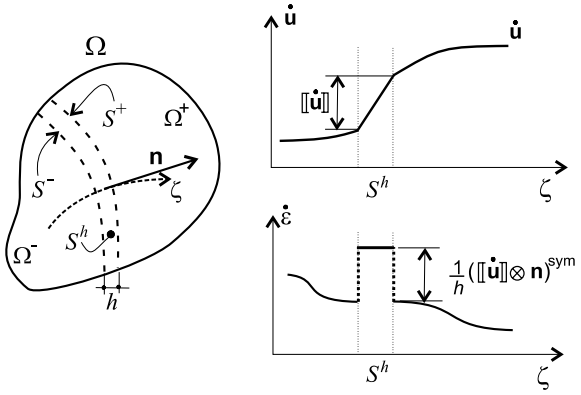

Fig. 3. Regularized strong discontinuity kinematics.

where $\mu_S^h(\mathbf{x})$ is a collocation function on S^H. The regularized version of Eq. (4) now reads:

$$\dot{\boldsymbol{\varepsilon}}(\mathbf{x},t) = \underbrace{\dot{\bar{\boldsymbol{\varepsilon}}}(\mathbf{x},t)}_{\text{regular (bounded)}} + \underbrace{\frac{1}{h}\mu_S^h([\![\dot{\mathbf{u}}]\!]\otimes\mathbf{n})^S}_{\text{singular (unbounded as } h\to 0)} \quad . \tag{6}$$

The kinematics of Eq. (6) allows one to introduce a new ingredient, which becomes necessary for purposes of modelling the fracture process zone described in Section 2 and Fig. 1. We shall consider the possibility for the bandwidth of the discontinuity interface, h, to be *different from zero* ($h \neq 0$) so that, according to Eq. (6), the strain field is bounded and it is characterized in terms of an *apparent jump* measured as the difference of the displacement field at both sides of the band (see Fig. 3) $[\![\mathbf{u}]\!] = \mathbf{u}|_{\mathbf{x}\in S^+} - \mathbf{u}|_{\mathbf{x}\in S^-}$. We will name such situation *weak discontinuity* and, for the subsequent analysis, we will characterize it by an slight modification in Eq. (5) neglecting the bandwidth h in front of the typical size of the body Ω and, therefore, considering the discontinuity surface S instead of the discontinuity band S^h in such equation i.e.

$$\text{Weak–strong discontinuity kinematics} \begin{cases} \dot{\boldsymbol{\varepsilon}}(\mathbf{x},t) = \dot{\bar{\boldsymbol{\varepsilon}}}(\mathbf{x},t) + \frac{1}{h}\mu_S([\![\dot{\mathbf{u}}]\!]\otimes\mathbf{n})^S; \quad \mu_S(\mathbf{x}) = \begin{cases} 1 & \mathbf{x}\in S, \\ 0 & \mathbf{x}\in \Omega\setminus S, \end{cases} \\ \text{Weak discontinuity: } h \neq 0, \\ \text{Strong discontinuity: } h \to 0, \end{cases} \tag{7}$$

In this context, the process of formation of a strong discontinuity at a material point $\mathscr{P}$ of the body can be modelled as a weak discontinuity that collapses into a strong discontinuity at a certain time of the deformation process (see Fig. 4). At time t_B (from now on the *bifurcation time*) the stress–strain field bifurcates, according to the kinematics of Eq. (7), [4] with $[\![\dot{\mathbf{u}}]\!] \neq \mathbf{0}$, resulting in a localization band of bandwidth h_B (see Fig. 4(a)) which characterizes the onset of a weak discontinuity. At subsequent times the bandwidth decreases ruled by a certain (material property) bandwidth evolution law (see Fig. 4(d)) up to reach a null value (for computational purposes, a very small parameter k) [5] at time t_{SD} (from now on the

[4] This bifurcation consists of increasing the strains inside the band and decreasing them outside. In consequence the strains begin to *localize*.

[5] This minimum bandwidth value, k, should be as small as permitted by the machine precision.

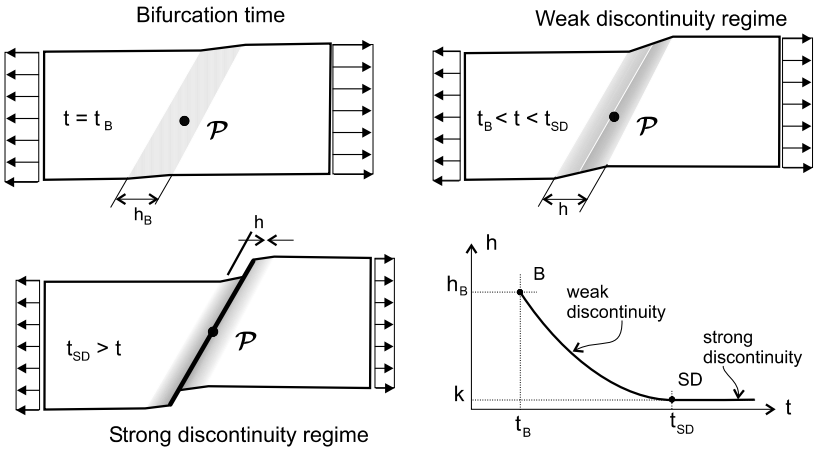

Fig. 4. Onset and development of a discontinuity: bandwidth law.

strong discontinuity time) which characterizes the onset of the strong discontinuity. Therefore, during the time interval $[t_B, t_{SD}]$ a weak discontinuity appears at $\mathscr{P}$ which collapses into a strong discontinuity at time $t = t_{SD}$. Finally for $t \geqslant t_{SD}$ a full strong discontinuity develops. More details can be found in Refs. [20,21] and [24].

The kinematics described so far in Eq. (7) and the devised mechanism of formation of a strong discontinuity in Fig. 4, match the fracture process scheme in Fig. 1. Now, one can characterize the different zones of the fracture process zone as

- Material points that have already reached the non-linear behaviour (damage, plastic, etc.) but not having bifurcated yet. They define a zone with continuous non-linear behaviour (diffuse failure zone in Fig. 1).
- Material points that have already bifurcated and, thus, experiencing a weak discontinuity kinematics, $[\![\mathbf{u}]\!] \neq \mathbf{0}$, with a non-zero bandwidth (weak discontinuity zone in Fig. 1).
- Material points that have reached the strong discontinuity regime, $h = k \simeq 0$ (strong discontinuity zone in Fig. 1).

In this context, Eq. (7) can be integrated along time (for $t > t_{SD}$) as follows:

$$\boldsymbol{\varepsilon}(\mathbf{x},t) = \int_0^t \dot{\boldsymbol{\varepsilon}}(\mathbf{x},t)\,\mathrm{d}t = \underbrace{\int_0^t \dot{\bar{\boldsymbol{\varepsilon}}}(\mathbf{x},t)\,\mathrm{d}t + \int_{t_B}^{t_{SD}} \frac{1}{h(t)}\mu_S([\![\dot{\mathbf{u}}]\!]\otimes\mathbf{n})^S\,\mathrm{d}t}_{\boldsymbol{\varepsilon}_{SD}\ \text{(bounded)}} + \underbrace{\int_{t_{SD}}^t \frac{1}{k}\mu_S([\![\dot{\mathbf{u}}]\!]\otimes\mathbf{n})^S\,\mathrm{d}t}_{\frac{1}{k}\mu_S(\boldsymbol{\beta}\otimes\mathbf{n})^S}, \tag{8}$$

where the material surface character of $S(\dot{\mathbf{n}} = \mathbf{0})$ has been considered. Therefore,

$$\boldsymbol{\varepsilon}(\mathbf{x},t) = \underbrace{\boldsymbol{\varepsilon}_{SD}}_{\text{(bounded)}} + \underbrace{\mu_S \frac{1}{k}(\boldsymbol{\beta}\otimes\mathbf{n})^S}_{\substack{\text{(unbounded)}\\ \text{for } k\to 0}}, \tag{9a}$$

$$\boldsymbol{\beta}(\mathbf{x},\mathbf{t}) = [\![\mathbf{u}]\!](\mathbf{x},t) - [\![\mathbf{u}]\!](\mathbf{x},t_{SD}) \quad \forall t \geqslant t_{SD}, \tag{9b}$$

where $\boldsymbol{\beta}$ is the incremental displacement jump since the strong discontinuity onset at t_{SD}. Again, the split of the strain field into bounded and unbounded counterparts is emphasized in Eq. (9).

3.2. Traction continuity: stress boundedness

Let us denote $\boldsymbol{\varepsilon}_{\Omega\setminus S} = \boldsymbol{\varepsilon}|_{\mathbf{x}\in\Omega\setminus S}$ and $\boldsymbol{\sigma}_{\Omega\setminus S} = \boldsymbol{\sigma}|_{\mathbf{x}\in\Omega\setminus S}$ stresses at the continuous bulk of the body, and $\boldsymbol{\varepsilon}_S = \boldsymbol{\varepsilon}|_{\mathbf{x}\in S}$ and $\boldsymbol{\sigma}_S = \boldsymbol{\sigma}|_{\mathbf{x}\in S}$ those entities evaluated at the discontinuity interface S. A crucial point in the present scenario is to postulate the traction continuity across the discontinuity interface S. This condition can be stated, in total and rate forms, as

$$\text{Traction continuity} \rightarrow \left\{ \begin{array}{l} \boldsymbol{\sigma}^{+}_{\Omega\setminus S}\cdot\mathbf{n} = \boldsymbol{\sigma}^{-}_{\Omega\setminus S}\cdot\mathbf{n} = \boldsymbol{\sigma}_S\cdot\mathbf{n} = \mathscr{T}(\mathbf{x},t) \\ \dot{\boldsymbol{\sigma}}^{+}_{\Omega\setminus S}\cdot\mathbf{n} = \dot{\boldsymbol{\sigma}}^{-}_{\Omega\setminus S}\cdot\mathbf{n} = \dot{\boldsymbol{\sigma}}_S\cdot\mathbf{n} = \dot{\mathscr{T}}(\mathbf{x},t) \end{array} \right. \quad \forall \mathbf{x}\in S\ \forall t\in[0,T], \tag{10a,b}$$

where $\boldsymbol{\sigma}^{+}_{\Omega\setminus S} = \boldsymbol{\sigma}_{\Omega\setminus S}|_{\mathbf{x}\in\partial\Omega^{+}\cap S}$ and $\boldsymbol{\sigma}^{-}_{\Omega\setminus S} = \boldsymbol{\sigma}_{\Omega\setminus S}|_{\mathbf{x}\in\partial\Omega^{-}\cap S}$. The first equality in Eqs. (10a) and (10b) is classically postulated in continuum mechanics, and the second is a natural extension motivated by the adopted continuum format that takes into consideration the material points in the discontinuity interface S. Eq. (10) leads to fundamental conclusions about the boundedness of the stress and stress-like fields, $\boldsymbol{\sigma}_S$ and q_S, through the following reasoning:

1. The constitutive model (1) returns bounded stresses for bounded input strains. Since, according to Eq. (6), the strains at the bulk $\boldsymbol{\varepsilon}_{\Omega\setminus S} = \bar{\boldsymbol{\varepsilon}}$ are bounded, so must be the stresses $\boldsymbol{\sigma}_{\Omega\setminus S}$ and the corresponding tractions $\mathscr{T} = \boldsymbol{\sigma}^{+}_{\Omega\setminus S}\cdot\mathbf{n} = \boldsymbol{\sigma}^{-}_{\Omega\setminus S}\cdot\mathbf{n}$ in Eq. (10a).
2. In order to assure the condition above, *the stresses at the discontinuity interface $\boldsymbol{\sigma}_S$ must be bounded*. Otherwise boundedness of $\mathscr{T} = \boldsymbol{\sigma}_S\cdot\mathbf{n}$ could not be guaranteed in Eq. (10a) for any value of $\mathbf{n}$. From the rate version of the traction continuity (10b) we conclude, from a similar reasoning, that *$\dot{\boldsymbol{\sigma}}_S$ is also bounded.*
3. As for *the stress-like variable* $q_S = q|_{\mathbf{x}\in S}$ in Eq. (1g) *it is bounded by construction* ($q\in[0,\sigma_u]$). In addition, from the persistency condition (1i) and the bounded character of the uniaxial equivalent stress $\phi(\boldsymbol{\sigma})$ in Eq. (1f)

$$\lambda_S\dot{f}_S = 0 \Rightarrow \left\{ \begin{array}{l} \lambda_S = 0 \rightarrow \dot{q}_S = H\lambda_S = 0 \\ \lambda_S \neq 0 \rightarrow \dot{f}_S = \underbrace{\partial_\sigma\phi(\boldsymbol{\sigma}_S):\dot{\boldsymbol{\sigma}}_S}_{\text{(bounded)}} - \dot{q}_S = 0 \end{array} \right\} \Rightarrow \dot{q}^S = \text{bounded}.$$

Therefore, we conclude the bounded character of $\boldsymbol{\sigma}_S$, $\dot{\boldsymbol{\sigma}}_S$, q_S and $\dot{q}_S$. This fact will be taken into consideration in next sections.

3.3. Discrete free energy

Let us now consider, at the strong discontinuity regime ($t\geqslant t_{\mathrm{SD}}; h = k\rightarrow 0$), the density of free energy $\Psi|_{\mathbf{x}\in S} = \Psi_S$ of Eq. (1a) in the discontinuity interface S, and its surface counterpart $\overline{\Psi}$, from now on termed *discrete free energy* which, in the context of the regularization procedure sketched in Fig. 3, can be written as

$$\bar{\psi}(\boldsymbol{\varepsilon}_S(\boldsymbol{\varepsilon}_{\mathrm{SD}},\boldsymbol{\beta}),\boldsymbol{\varepsilon}^{(i)}_S,q_S) = \frac{\text{free energy}}{\text{unit surface}} = \underbrace{\frac{\text{free energy}}{\text{unit volume}}}_{\psi_S}\cdot\underbrace{\frac{\text{unit volume}}{\text{unit surface}}}_{h} = \lim_{h\rightarrow 0} h\psi(\boldsymbol{\varepsilon}(\boldsymbol{\varepsilon}_{\mathrm{SD}},\boldsymbol{\beta}),\varepsilon^{(i)}_S,q_S), \tag{11}$$

where the functional dependences $\psi(\boldsymbol{\varepsilon},\boldsymbol{\varepsilon}^{(i)},q)$ and $\boldsymbol{\varepsilon}_S(\boldsymbol{\varepsilon}_{\mathrm{SD}},\boldsymbol{\beta})$, stated in Eqs. (1a) and (9), have been emphasized. These dependences can be reduced by the following algebraic procedure:

$$\frac{\partial\bar{\psi}}{\partial\boldsymbol{\varepsilon}_{\mathrm{SD}}} = \lim_{h\rightarrow 0} h\frac{\partial\psi_S}{\partial\boldsymbol{\varepsilon}_{\mathrm{SD}}} = \lim_{h\rightarrow 0} h\underbrace{\frac{\partial\psi_S}{\partial\boldsymbol{\varepsilon}_S}}_{\boldsymbol{\sigma}_S}:\underbrace{\frac{\partial\boldsymbol{\varepsilon}_S}{\partial\boldsymbol{\varepsilon}_{\mathrm{SD}}}}_{\mathbf{I}} = \lim_{h\rightarrow 0} h\underbrace{\boldsymbol{\sigma}_S}_{\text{(bounded)}} = \mathbf{0}, \tag{12a}$$

$$\frac{\partial\bar{\psi}}{\partial\boldsymbol{\varepsilon}_S^{(i)}} = \lim_{h\to 0} h \underbrace{\frac{\partial\psi_S}{\partial\boldsymbol{\varepsilon}_S^{(i)}}}_{-\boldsymbol{\sigma}_S} = -\lim_{h\to 0} h \underbrace{\boldsymbol{\sigma}_S}_{\text{(bounded)}} = \mathbf{0}, \tag{12b}$$

where Eqs. (9a) and (1b), and the bounded character of $\boldsymbol{\sigma}_S$ stated in Section 3.2 have been considered. From Eqs. (11) and (12) the functional dependences of $\bar{\psi}$ can be stated as $\bar{\psi}(\boldsymbol{\beta}, q_S)$. Let us now define the *discrete internal variable* $\bar{\alpha}$ as

$$\bar{\alpha} = 0, \quad t \in [0, t_{\text{SD}}] \tag{13a}$$

$$\bar{\alpha} = h(\alpha_S - \alpha_S^{\text{SD}}) \Rightarrow \begin{cases} \alpha_S = \alpha_S^{\text{SD}} + \frac{1}{h}\bar{\alpha} \\ \dot{\alpha}_S = \frac{1}{h}\dot{\bar{\alpha}} \end{cases} \forall t \geqslant t_{\text{SD}}. \tag{13b}$$

where $\alpha_S^{\text{SD}} = \alpha_S(t)|_{t=t_{\text{SD}}}$. Let us now define the *discrete plastic/damage multiplier* $\bar{\lambda}$ as

$$\bar{\lambda} = \dot{\bar{\alpha}} = h\dot{\alpha}_S = h\lambda, \tag{14}$$

where, Eqs. (1e) and (13b) have been considered. Now, taking into consideration Eqs. (1b) and (9a) and (13) one can write

$$\frac{\partial\bar{\psi}(\boldsymbol{\beta}, q_S)}{\partial\boldsymbol{\beta}} = \lim_{h\to 0} h \underbrace{\frac{\partial\psi_S}{\partial\boldsymbol{\varepsilon}}}_{\boldsymbol{\sigma}_S} : \underbrace{\frac{\partial\boldsymbol{\varepsilon}}{\partial\boldsymbol{\beta}}}_{\frac{1}{h}(\mathbf{1}\otimes\mathbf{n})^S} = \lim_{h\to 0} h \frac{1}{h} \underbrace{\boldsymbol{\sigma}_S \cdot \mathbf{n}}_{\mathscr{T}} = \mathscr{T}, \tag{15a}$$

$$\frac{\partial\bar{\psi}(\boldsymbol{\beta}, q_S)}{\partial q_S} = \lim_{h\to 0} h \underbrace{\frac{\partial\psi_S}{\partial q_S}}_{\alpha_S} \lim_{h\to 0} h \underbrace{\alpha_S}_{\frac{1}{h}\bar{\alpha}} = \lim_{h\to 0} h \frac{1}{h}\bar{\alpha} = \bar{\alpha}, \tag{15b}$$

which qualifies the discrete free energy $\bar{\psi}(\boldsymbol{\beta}, q_S)$ as a potential for the tractions $\mathscr{T}$ and the discrete internal variable $\bar{\alpha}$, in terms of their respective conjugate variables $\boldsymbol{\beta}$ and q_S.

Remark 1. Eq. (15) hints at a crucial consequence of the insertion of strong discontinuity kinematics into continuum (stress–strain) models: the projection of these continuum models into discrete (traction–displacement jump) ones. In fact, the discrete free energy $\bar{\psi}$, obtained as the surface counterpart of the continuum free energy density ψ_S, turns into a potential for the nominal traction $\mathscr{T} = \boldsymbol{\sigma}_S \cdot \mathbf{n}$, with respect to the incremental jump $\boldsymbol{\beta}$, as shown in Eq. (15a). This suggests that a discrete constitutive model $\mathscr{T} = \mathscr{T}(\boldsymbol{\beta}, q_S)$ can be derived from that discrete free energy and, therefore, from the inclusion of a strong discontinuity kinematics in the original continuum model (1).

In a similar manner one can compute the surface dissipation $\overline{\mathscr{D}}$ as the discrete counterpart of the volumic dissipation $\mathscr{D}$ of Eq. (1j) at the discontinuity interface S:

$$\bar{\mathscr{D}} = \lim_{h\to 0} h\mathscr{D}_S = \lim_{h\to 0} h(\boldsymbol{\sigma}_S : \dot{\boldsymbol{\varepsilon}}_S - \dot{\Psi}_S) = \lim_{h=k\to 0} \left[h \left(\underbrace{\boldsymbol{\sigma}_S : \dot{\boldsymbol{\varepsilon}}_{\text{SD}}}_{\text{(bounded)}} + \boldsymbol{\sigma}_S : \frac{1}{k}(\dot{\boldsymbol{\beta}} \otimes \mathbf{n}) \right)^S \right] - \underbrace{\lim_{h\to 0} h(\dot{\Psi}_S)}_{\dot{\bar{\psi}}}$$

$$= \underbrace{\boldsymbol{\sigma}_S : (\dot{\boldsymbol{\beta}} \otimes \mathbf{n})^S}_{\mathscr{T}\cdot\dot{\boldsymbol{\beta}}} - \dot{\bar{\psi}}(\boldsymbol{\beta}, q_S) = \mathscr{T} \cdot \dot{\boldsymbol{\beta}} - \underbrace{\frac{\partial\bar{\psi}}{\partial\beta}}_{\mathscr{T}} \cdot \dot{\boldsymbol{\beta}} - \underbrace{\frac{\partial\bar{\psi}}{\partial q_S}}_{\bar{\alpha}} \dot{q}_S = \bar{\alpha}\dot{q}_S, \tag{16}$$

where Eqs. (9a) (in rate form), (11) and (15a) and (15b) have been considered. In summary, the *discrete surface dissipation density* $\overline{\mathscr{D}}$ can be written as

$$\overline{\mathscr{D}} = \mathscr{T} \cdot \dot{\boldsymbol{\beta}} - \dot{\bar{\psi}} = -\bar{\alpha}\dot{q}_S \geqslant 0. \tag{17}$$

3.4. Softening modulus regularization: discrete softening modulus

Let us consider the continuum softening law (1g) at the discontinuity interface S for the strong discontinuity regime ($t \geqslant t_{\mathrm{SD}}$; $h = k \to 0$). From the rate version of Eq. (13) one obtains

$$\begin{cases} \dot{q}_S = H(q_S)\dot{\alpha}_S \\ \dot{\alpha}_S = \frac{1}{h}\dot{\bar{\alpha}} = \frac{1}{k}\dot{\bar{\alpha}} \end{cases} \Rightarrow \underbrace{\dot{q}_S}_{\text{(bounded)}} = H(q_S)\dot{\alpha}_S = \underbrace{H(q_S)\frac{1}{h}}_{\overline{H}(q_S)}\dot{\bar{\alpha}}, \tag{18}$$

which states the discrete counterpart of the softening law as

$$\text{Discrete softening law} \to \underbrace{\dot{q}_S}_{\text{(bounded)}} = \overline{H}(q_S)\ \underbrace{\dot{\bar{\alpha}}}_{\text{(bounded)}}, \tag{19}$$

where the *discrete softening modulus* $\overline{H}$ is obtained, from Eq. (18), in terms of the continuum softening modulus H

$$\text{Softening regularization condition} \to \overline{H} = \frac{1}{h}H \Rightarrow H = h\overline{H}. \tag{20}$$

Notice that, as emphasized in Eq. (19), $\dot{q}_S$ and $\dot{\bar{\alpha}}$ are bounded and, therefore, so is the discrete softening modulus $\overline{H} \leqslant 0$ that can be immediately related to material properties like the peak stress σ_u and *the fracture energy* G_{f} [3]. In fact, integration of the surface dissipation density (17) along the dissipation process, leads to the concept of fracture energy expressed as the surface density of energy dissipated in the whole process of formation of a fracture

$$G_{\mathrm{f}} = \int_0^\infty \overline{\mathscr{D}}\,\mathrm{d}t = \int_0^\infty -\bar{\alpha}\dot{q}_S\,\mathrm{d}t = \int_0^\infty q_S\dot{\bar{\alpha}}\,\mathrm{d}t - \underbrace{\int_0^\infty \frac{\mathrm{d}}{\mathrm{d}t}(q_S\bar{\alpha})\,\mathrm{d}t}_{=0} = \int_0^\infty q_S\,\mathrm{d}\bar{\alpha} = A(\sigma_u, \overline{H}), \tag{21}$$

where A stands for the area under the softening curve $q_S(\bar{\alpha})$ in the space $(q_S, \bar{\alpha})$ and Eq. (1g) ($q_S|_{t=\infty} = 0$) and (13a) ($\bar{\alpha}|_{t=\infty} = 0$) have been considered. Therefore, in this setting the discrete softening modulus $\overline{H}$ *becomes the actual material property* instead of the standard continuum softening modulus H.

Remark 2. The softening regularization condition (19) has been strictly deduced for the strong discontinuity regime ($t \geqslant t_{\mathrm{SD}}$; $h = k \to 0$). However, in the context of the variable bandwidth model of Section 3.1 it will also be assumed for the entire discontinuity regime ($t \geqslant t_{\mathrm{B}}$) in order to assure a smooth transition from the weak to the strong discontinuity regimes.

Remark 3. From Eq. (20) it emerges, for the strong discontinuity regime, the (k-regularized) null value of the continuum softening modulus ($H \to 0$ as $h \to 0$). This fact has been some times related to the "distributional character of the inverse of H".

3.5. Complementary energy potentials: strong discontinuity conditions

Let us now consider the complementary free energy of the constitutive model, obtained as the Legendre transformation of the free energy Ψ in Eq. (1a)

$$G(\boldsymbol{\sigma},\alpha) = \boldsymbol{\sigma} : (\boldsymbol{\varepsilon} - \boldsymbol{\varepsilon}^{(i)}) + q\alpha - \Psi(\boldsymbol{\varepsilon} - \boldsymbol{\varepsilon}^{(i)}, q) \tag{22}$$

and, therefore

$$\partial_{\boldsymbol{\sigma}} G(\boldsymbol{\sigma},\alpha) = (\boldsymbol{\varepsilon} - \boldsymbol{\varepsilon}^{(i)}), \tag{23a}$$

$$\partial_{\alpha} G(\boldsymbol{\sigma},\alpha) = q. \tag{23b}$$

The discrete counterpart of G shall be the *discrete surface complementary energy* $\overline{G}$ defined as

$$\overline{G} = \lim_{h\to 0} hG(\boldsymbol{\sigma}_S, \alpha_S). \tag{24}$$

Substitution of Eqs. (24) and (9a) into Eq. (22) for the strong discontinuity regime ($t \geqslant t_{\mathrm{SD}}$; $h = k \to 0$) leads to

$$\begin{aligned}\frac{\partial \overline{G}}{\partial \boldsymbol{\sigma}} &= \lim_{h=k\to 0} \frac{\partial hG(\boldsymbol{\sigma}_S,\alpha_S)}{\partial \boldsymbol{\sigma}} = \lim_{h=k\to 0} h(\boldsymbol{\varepsilon} - \boldsymbol{\varepsilon}_S^{(i)}) = \lim_{h=k\to 0} h\left(\underbrace{\boldsymbol{\varepsilon}_{\mathrm{SD}}}_{\text{bounded}} + \frac{1}{k}(\boldsymbol{\beta}\otimes\mathbf{n})^S - \boldsymbol{\varepsilon}_S^{(i)} \right) \\ &= (\boldsymbol{\beta}\otimes\mathbf{n})^S - \lim_{h\to 0} h\boldsymbol{\varepsilon}_S^{(i)} \Rightarrow \lim_{h\to 0} h\left[\frac{\partial G(\boldsymbol{\sigma}_S,\alpha_S)}{\partial \boldsymbol{\sigma}} + \boldsymbol{\varepsilon}^{(i)}(\boldsymbol{\sigma}_S,\alpha_S) \right] = (\boldsymbol{\beta}\otimes\mathbf{n})^S. \end{aligned} \tag{25}$$

Let us consider the orthonormal basis $\{\hat{\mathbf{e}}_1 \equiv \mathbf{n}, \hat{\mathbf{e}}_2, \hat{\mathbf{e}}_3\}$. Due to the particular rank-one structure of the right-hand side of Eq. (25), components $(\cdot)_{22}$, $(\cdot)_{23}$ and $(\cdot)_{33}$ of such equation, in that basis, read

$$\begin{aligned}&\text{Strong discontinuity conditions} \rightarrow \lim_{h\to 0} h\left[\frac{\partial G(\boldsymbol{\sigma}_S,\alpha_S)}{\partial \sigma_{ij}} + \boldsymbol{\varepsilon}_{ij}^{(i)}(\boldsymbol{\sigma}_S,\alpha_S) \right] = 0, \\ &\qquad\qquad i,j \in \{2,3\} \quad \forall t \geqslant t_{\mathrm{SD}}, \end{aligned} \tag{26}$$

which constitutes a set of three equations that must be fulfilled at the strong discontinuity regime. They can be understood as a *restriction on the stress states liable to happen at the discontinuity interface for* $t > t_{\mathrm{SD}}$.

Remark 4. Since the three strong discontinuity conditions (26) involve the six components of $\boldsymbol{\sigma}_S$, they implicitly define the components σ_{22}, σ_{33}, σ_{13} as functions of the remaining components of $\boldsymbol{\sigma}_S$ i.e.: the components of the traction $\mathscr{T} = \boldsymbol{\sigma}_S \cdot \mathbf{n} \equiv [\sigma_{11}, \sigma_{12}, \sigma_{13}]^{\mathrm{T}}$. Therefore the stress state at the strong discontinuity regime can be written as

$$\boldsymbol{\sigma}_S = \Sigma_S(\mathscr{T}) \quad \forall t \geqslant t_{\mathrm{SD}}, \tag{27}$$

which states that the stress state at the discontinuous interface S is driven by its $\mathbf{n}$-projection ($\boldsymbol{\sigma}_S \cdot \mathbf{n}$), i.e. the traction $\mathscr{T}$.

For the class of constitutive models specified in Eq. (2) it can be easily proven from Eq. (26) that the following strong discontinuity conditions result:

	$\partial_{\boldsymbol{\sigma}_S} G(\boldsymbol{\sigma}_S,\alpha_S)$	$\dot{\boldsymbol{\varepsilon}}^{(i)}$	Strong discontinuity conditions
Elastoplastic models	$\underbrace{\mathbf{C}^{-1} : \boldsymbol{\sigma}_S}_{\text{(bounded)}}$	$\dot{\alpha}_S \mathbf{m}(\boldsymbol{\sigma}_S)$	$m_{22}(\boldsymbol{\sigma}_S) = 0$ $m_{33}(\boldsymbol{\sigma}_S) = 0$ $m_{23}(\boldsymbol{\sigma}_S) = 0$
Isotropic damage models	$\frac{1}{1-d(\alpha_S)}\mathbf{C}^{-1} : \boldsymbol{\sigma}_S$	$\mathbf{0}$	$[\mathbf{C}^{-1} : \boldsymbol{\sigma}_S]_{22} = 0$ $[\mathbf{C}^{-1} : \boldsymbol{\sigma}_S]_{33} = 0$ $[\mathbf{C}^{-1} : \boldsymbol{\sigma}_S]_{23} = 0$

. (28)

Remark 5. Now the variable bandwidth model of Section 3.1 and Fig. 4 can be regarded as a way to delay the onset of the strong discontinuity regime up to the, necessary, fulfillment of the strong discontinuity conditions (28) or, conversely, a procedure to smoothly induce the strong discontinuity conditions since they will not, in general, be fulfilled at the bifurcation time t_{B}.

3.6. Discrete constitutive model

The elements developed in Sections 3.3–3.5 can be now put together to render the following *discrete constitutive model induced, from the continuum constitutive model* (1), *by the strong discontinuity kinematics* (9):

$$\text{Free energy:} \quad \overline{\psi}(\boldsymbol{\beta}, q_S), \tag{29a}$$

$$\text{Constitutive equations:} \quad \begin{cases} \mathscr{T} = \partial_{\boldsymbol{\beta}} \overline{\psi}(\boldsymbol{\beta}, q_S), \\ \bar{\alpha} = \partial_{q_S} \overline{\psi}((\boldsymbol{\beta}, q_S), \end{cases} \tag{29b,c}$$

$$\text{Internal variable evolution:} \quad \dot{\bar{\alpha}} = \bar{\lambda}, \tag{29d}$$

$$\text{Yield/damage function:} \quad \mathscr{F}(\mathscr{T}, q_S) \equiv \phi(\boldsymbol{\sigma}(\mathscr{T})) - q_S, \tag{29e}$$

$$\text{Softening law:} \quad \begin{cases} \dot{q}_S = \overline{H}(q_S)\dot{\bar{\alpha}} & \overline{H} \leqslant 0, \\ q_S \in [0, q_{\mathrm{SD}}] & q_{\mathrm{SD}} := q_S|_{t=t_{\mathrm{SD}}}, \end{cases} \tag{29f,g}$$

$$\text{Loading/unloading conditions:} \quad \bar{\lambda} \geqslant 0 \quad \mathscr{F} \leqslant 0 \quad \bar{\lambda}\mathscr{F} = 0, \tag{29h}$$

$$\text{Persistency conditions:} \quad \bar{\lambda}\dot{\mathscr{F}} = 0 \quad \textit{if } \mathscr{F} = 0, \tag{29i}$$

$$\text{Surface dissipation:} \quad \overline{\mathscr{D}} = \mathscr{T} \cdot \dot{\boldsymbol{\beta}} - \dot{\overline{\psi}} = -\bar{\alpha}\dot{q}_S. \tag{29j}$$

Remark 6. At the onset of the strong discontinuity regime ($t = t_{\mathrm{SD}}$) the incremental jump is null ($\boldsymbol{\beta}_{\mathrm{SD}} = \mathbf{0}$) according to its definition in Eq. (9b) whereas $\mathscr{T}_{\mathrm{SD}}$ is not. Therefore the initial secant modulus $\mathbf{Q}_{\mathrm{SD}}$ of the discrete model (29) defined through $\mathscr{T}_{\mathrm{SD}} = \mathbf{Q}_{\mathrm{SD}} \cdot \boldsymbol{\beta}_{\mathrm{SD}}$ is infinite. This fact qualifies the projected discrete model as a "rigid model" a feature frequently required, on physical grounds, to "ad hoc" devised models for cohesive interfaces.

4. Computational issues

A variety of computational schemes can be inserted in the strong discontinuity scenario presented in Section 3. As for the spatial discretization, both the boundary element and (more widely) the finite element methods can be used for those purposes. In addition some particular aspects as propagation of the discontinuity interfaces require the development of specific techniques that are presented in next sections.

4.1. Finite elements with embedded discontinuities

In the finite element simulation context, it should be expected that the best performance is provided by those finite elements specifically devised for the considered problem, i.e. finite elements equipped with deformation modes liable to capture the displacements jumps that characterize the strong discontinuities.

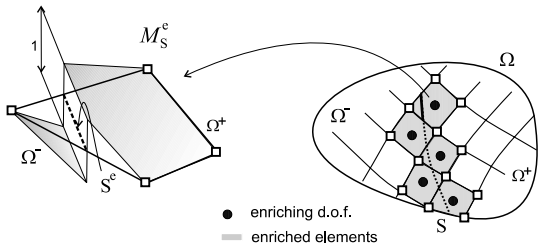

Fig. 5. Elemental enrichment mode M_S^e.

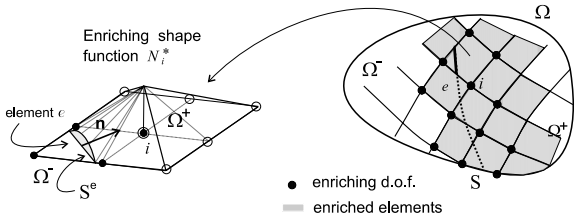

Fig. 6. Nodal enrichment mode.

This has motivated the development of the so called *finite element with embedded discontinuities*. They are build up on the basis of a standard finite element which is enriched with additional displacement/strain modes that make it compatible with the strong discontinuity kinematics of Eq. (7). In this context, two different families can be distinguished:

- *Elemental enrichment* (see for instance [1,9,13,18]). The support of the enriching discontinuity mode is elemental (see Fig. 5) and, in consequence, the additional internal discontinuous degrees of freedom can be condensed at the elemental level. The displacement jump is element-wise constant.
- *Nodal enrichment* (see for instance [4,33]). The support of the enriching discontinuous mode is the same than for the nodal shape functions of the underlying element (see Fig. 6). The regular nodes of the enriched set of elements are increased with additional degrees of freedom (two per node in 2D cases) whose interpolation provides a (continuous across the elements) jump displacement field. The additional degrees of freedom cannot be condensed at element level.

Detailed description of finite elements with embedded discontinuities is out of the scope of this work. The interested reader is addressed to Ref. [22] for that purpose.

4.2. Discontinuity tracking

Constructing the additional discontinuous modes for the finite elements with embedded discontinuities presented in Section 4.1, requires the determination of the set of enriched elements (see Figs. 5 and 6) and the position of the discontinuity path inside every element of that set. The strategies devoted to predicting and capturing the geometrical position of those discontinuity paths [6] will be from now on termed *discontinuity tracking algorithms*. They are based on the knowledge of the following ingredients for every material point $\mathscr{P}$ of the body [25]:

[6] Along this section the term *discontinuity* refers to the appearance of both types of discontinuities (weak and strong) discussed in Section 3.1.

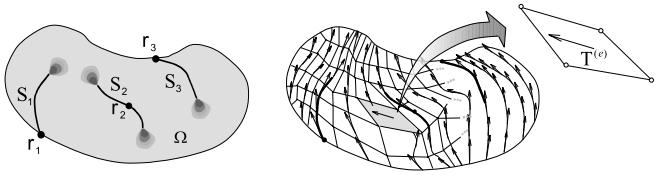

Fig. 7. Discontinuity paths.

(a) A *local failure criterion* to signal the onset of the discontinuity. In the simplest cases this condition corresponds to the end of the elastic regime in the bulk through the fulfillment of some yield or damage criterion. On a more rigorous theoretical basis, and in the spirit of the mechanism considered in Section 3.1, propagation can be triggered [7] the first time $t_{\mathrm{B}}(\mathbf{x})$ that a material bifurcation criterion (loss of strong ellipticity) is fulfilled [23,27,34].
(b) A *direction of propagation*. This direction is given either on a empirical basis (for instance, the propagation direction is made orthogonal to the maximum tensile stress) or it is supplied by more sophisticated material bifurcation analyses [23,27].

On this basis let us consider a two-dimensional body Ω, liable to experience discontinuities that can take place along multiple discontinuity paths. Let us denote these discontinuity paths S_i $i \in \{1, \ldots n_{\mathrm{d}}\}$ where n_{d} is the number of them (see Fig. 7(a)). Each of them is characterized by its *root* r_i, the first material point (in a finite element context the first finite element) in S_i to fulfill the stated failure criterion. Let us also assume that for each material point $\mathbf{x}$ of Ω (every element of the finite element mesh) a propagation direction $\mathbf{T}(\mathbf{x}, t)$ (orthogonal to the normal $\mathbf{n}$ to the discontinuity path) is available at every time of the analysis $t \in [0, T]$.

In this scenario, tracking algorithms can be classified into [25]:

- *Propagation algorithms* (see Fig. 8): based on the recursive propagation from a *seed* [8] (root) to the neighbor elements by means of inter-element continuous straight segments. For a unique discontinuity path S, the algorithm, at every time step of the analysis, propagates from the root through the mesh by means of the following steps:
  1. As an element, e, is reached by S at the "input position" $I_S^{(e)}$ (see Fig. 8) the discontinuity path is propagated along the element, according to the direction of the propagation vector $\mathbf{T}(\mathbf{x}^{(e)}, t) \equiv \mathbf{T}^{(e)}(t)$, to determine the "output position" $O_S^{(e)}$.
  2. Position $O_S^{(e)}$, in the corresponding elemental side, is then transmitted to the neighbour element as a new input position $I_S^{(e+1)} \equiv O_S^{(e)}$.

     Steps 1 and 2 are repeated up to the boundary of Ω is reached at both ends of S. As an element, e, fulfills the local failure criterion, the corresponding points $I_S^{(e)}$ and $O_S^{(e)}$ are frozen and the elemental discontinuity path $S^{(e)}$ becomes part of the *consolidated discontinuity path*, no longer changed in subsequent time steps. [9]

[7] In a finite element computational setting, the numerical bifurcation must be artificially triggered at the considered finite element by imposing elastic behaviour (which should result into elastic unloading) at the bulk $\Omega \setminus S$ (regular sampling points) and inelastic loading at the discontinuity interface S (singular sampling points).

[8] The seed position can be either imposed by the user, or automatically computed as the first point (element) to fulfill the failure criterion.

[9] This makes the algorithm consistent with the *material character* of the discontinuity path ($\dot{\mathbf{n}} = \mathbf{0}$ for $t \geqslant t_{\mathrm{B}}$).

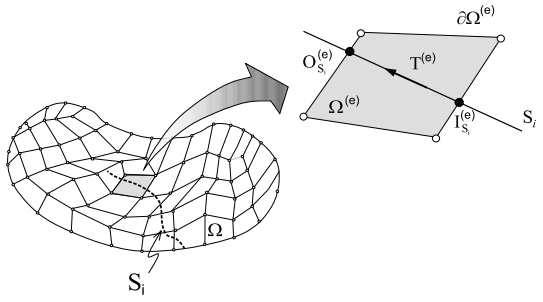

Fig. 8. Discontinuity tracking in a 2D problem using a propagation algorithm.

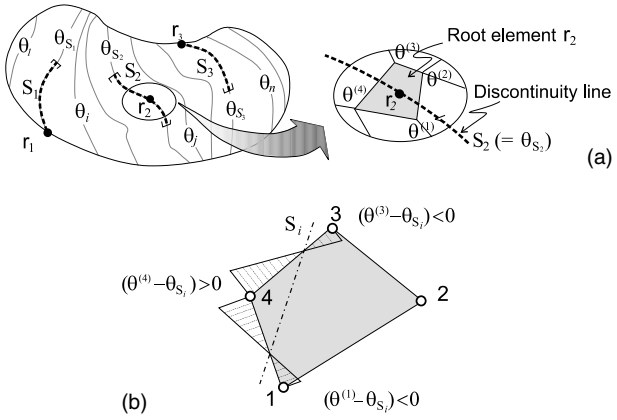

Fig. 9. Discontinuity tracking in a 2D problem using a global algorithm.

3. Once the position of S inside every element is known, the enriching modes of the selected finite element with embedded discontinuities are determined. Only those elements crossed by S are allowed to soften and to activate the discontinuity modes (7).
   Indeed, the algorithm requires handling of a *side-connectivity array* signaling those elements that share their sides with a given one, which breaks its local character and, therefore, its element level implementation in a finite element code. Although very intuitive and straightforward to implement, application of this type of algorithm to multiple discontinuity lines or to 3D cases is cumbersome. Recent *level set type* tracking algorithms, based on the propagation of moving surfaces ruled by an advection equation, could be a way to alleviate those problems [4,15].

- *Global tracking algorithms* (see Fig. 9). They aim at determining, at once, all the lines (in 2D), or surfaces (in 3D), candidates to be discontinuity paths and, then, identify among them the relevant (active) ones. The algorithm lies on the following steps:
  1. *Trace the envelopes of the propagation vector field.* Since, by construction, at every point $\mathbf{x}$ of the discontinuity paths S_i, the tangent has the sense of the propagation vector $\mathbf{T}(\mathbf{x}, t)$, then the S_i are segments of the family of curves enveloping the vector field $\mathbf{T}$ (see Fig. 9). Therefore, construction of the envelopes implicitly supplies all the S_i at time t. These envelopes can be described by a function $\theta(\mathbf{x})$ whose *level contours* ($\theta(\mathbf{x}) =$ constant) define all the possible discontinuity lines as (see Fig. 9)

$$S_i := \{\mathbf{x} \in \Omega; \quad \theta(\mathbf{x}) = \theta_{S_i}\} \tag{30}$$

for all the meaningful values of θ_{S_i}. In Section 4.3 a methodology for construction of such a family is provided. There $\theta(\mathbf{x})$ stands for the temperature field that is the solution of a stationary heat conduction problem and, therefore, S_i are segments of the isothermal lines. In the context of a thermal finite element analysis, this algorithm returns the nodal temperature values $\theta^{(k)}$.

2. *Identify the active discontinuity lines and their corresponding temperature level*. For every root element r_i, it is considered that the discontinuity path passes through its centroid (see Fig. 9(a)). Consequently, the corresponding temperature level is the average of the nodal temperatures for this root element

$$\theta_{S_i} = \frac{1}{n}\sum_{k=1}^{n} \theta^{(k)}, \tag{31}$$

where n stands for the number of nodes of the element (i.e.: $n = 3$, for linear triangles and $n = 4$ for linear quadrilaterals or tetrahedra). Then, temperatures θ_{S_i} $i = 1, \ldots n_{\mathrm{d}}$ (the *reference temperatures*) identify the corresponding discontinuity paths S_i.

3. *Determine the position of the discontinuity line inside a given element*. Once the nodal temperatures $\theta^{(k)}$ and the reference temperatures θ_{S_i} are known, the position of S_i inside a given element e can be immediately determined through the following algorithm (see Fig. 9(b)):

DATA:	Nodal temperatures of the element: $\theta^{(k)}$ Discontinuity line temperature: θ_{S_i}
ACTIONS:	
(1)	Determine the sides involving a change of sign of $(\theta^{(k)} - \theta_{S_i})$ at their vertices (sides crossed by S_i).
(2)	For every of these sides compute the position of S_i through linear interpolation.

(32)

Notice that no information from the neighbour elements is required in the preceding algorithm. This fact confers to the algorithm some interesting local character that can be exploited for implementation purposes.

4. *Identification of the root*, r_i of a new discontinuity path S_i. Any element e, satisfying for the first time the failure criterion, is declared the root r_{nd}, of a new discontinuity line S_{nd}, whenever it is not crossed by any discontinuity line S_i $i \in \{1, \ldots, n_{\mathrm{d}} - 1\}$ according to the previous algorithm.
5. *Freeze the consolidated part of the discontinuity paths*. Temperatures, at all the nodes of those elements fulfilling the local failure criterion (failed elements) at time t, are frozen for future time steps. This makes consistent the algorithm with the material character of consolidated discontinuity paths ($\dot{\mathbf{n}} = \mathbf{0}$).

4.3. Enveloping the propagation vector field: heat conduction-like problem

Let us now focus on a procedure to compute the envelopes of a vector field $\mathbf{T}(\mathbf{x}) = [T_x, T_y]^{\mathrm{T}}$ in a two-dimensional domain Ω. We shall assume that $\mathbf{T}(\mathbf{x})$ is a unit vector field, i.e.:

$$\mathbf{T} \cdot \mathbf{T} = \|\mathbf{T}\|^2 = 1, \tag{33}$$

whose sense shall be not relevant. The final goal is to obtain a function $\theta(\mathbf{x})$ whose level lines, defined by Eq. (30), are envelopes of $\mathbf{T}$. Since those contours are orthogonal to $\nabla\theta$, function $\theta(\mathbf{x})$ shall be the solution of the following partial differential equation:

$$\mathbf{T} \cdot \nabla\theta = \nabla\theta \cdot \mathbf{T} = \frac{\partial\theta}{\partial T} = 0, \quad \text{in } \Omega, \tag{34}$$

where $\frac{\partial\theta}{\partial T}$ stands for the directional derivative (in the direction of $\mathbf{T}$) of θ. As $\|\mathbf{T}\| \neq 0$, multiplying Eq. (34) times $\mathbf{T}$ one obtains

$$\frac{\partial\theta}{\partial T} = 0 \Longleftrightarrow \mathbf{T}\frac{\partial\theta}{\partial T} = (\mathbf{T}\otimes\mathbf{T})\cdot\boldsymbol{\nabla}\theta = \mathbb{K}\cdot\boldsymbol{\nabla}\boldsymbol{\theta} = \mathbf{0}, \tag{35a}$$

$$\mathbb{K} := \mathbf{T}\otimes\mathbf{T}. \tag{35b}$$

Now defining

$$\mathbf{q} = -\mathbb{K}\cdot\boldsymbol{\nabla}\boldsymbol{\theta}, \tag{36}$$

we consider the following boundary value problem:

Find: $\theta(\mathbf{x})$ satisfying:

$$\boldsymbol{\nabla}\cdot\mathbf{q} = 0 \quad \text{in } \Omega, \tag{37a}$$

$$\mathbf{q} = -\mathbb{K}\cdot\boldsymbol{\nabla}\boldsymbol{\theta} = -\mathbf{T}\frac{\partial\theta}{\partial T} \quad \text{in } \Omega, \tag{37b}$$

$$\mathbf{q}\cdot\boldsymbol{v} = (\boldsymbol{v}\cdot\mathbf{T})\frac{\partial\theta}{\partial T} = 0 \quad \text{on } \partial_q\Omega, \tag{37c}$$

$$\theta = \theta^*, \quad \text{on } \partial_\theta\Omega, \tag{37d}$$

where $\boldsymbol{v}$ is the outward normal to the boundary $\partial\Omega$ and $\partial_q\Omega$ and $\partial_\theta\Omega$ ($\partial_q\Omega\cup\partial_\theta\Omega = \partial\Omega$) stand, respectively, for those parts of the boundary $\partial\Omega$ were Newman and Dirichlet conditions are prescribed. If the Dirichlet boundary conditions (37d) are compatible with condition $\frac{\partial\theta}{\partial T} = 0$ then a solution satisfying

$$\theta(\mathbf{x}) \neq \text{constant}; \quad \frac{\partial\theta}{\partial T} = 0 \tag{38}$$

is the solution of problem (37) as can be checked by substitution of Eq. (38) in (37).

Problem (37) can be regarded as the steady-state heat conduction equation in Ω (see Fig. 10), for the case of no internal heat sources and null heat flux input ($\mathbf{q}_v = \mathbf{q}\cdot\boldsymbol{v} = \mathbf{0}$) on the boundary $\partial_q\Omega$ (adiabatic boundary). In this case θ plays the role of the temperature field, $\mathbf{q}$ is the conduction flux vector and $\mathbb{K}$ is a, point dependent, anisotropic thermal conductivity tensor given by

$$\mathbb{K}(\mathbf{T}(\mathbf{x})) = \mathbf{T}\otimes\mathbf{T} \equiv \begin{bmatrix} T_x^2 & T_xT_y \\ T_xT_y & T_y^2 \end{bmatrix}. \tag{39}$$

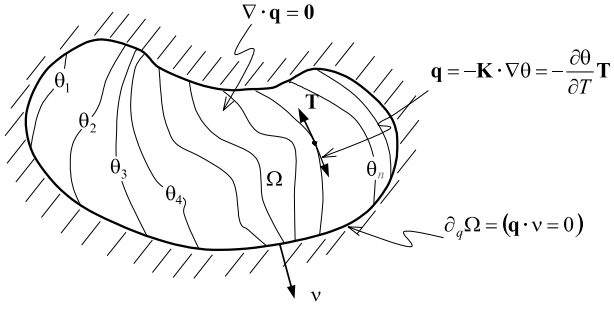

Fig. 10. Stationary heat conduction problem.

Remark 7. Notice that $\mathbb{K}(\mathbf{T}) = \mathbb{K}(-\mathbf{T})$ and that, as expected, the solution of problem (37) is only affected by the direction of the propagation vector field $\mathbf{T}$ and not by its sense.

Remark 8. The rank-one character of the conductivity tensor (39) can be source of ill-posedness of the heat conduction problem [10] (37). Indeed, since the flux vector $\mathbf{q}$, in Eq. (37b), has a null component in the direction $\mathbf{n}$ orthogonal to $\mathbf{T}$, from Eq. (38) the value of the directional derivative $\frac{\partial\theta}{\partial N} := \nabla\theta \cdot \mathbf{N}$ is not determined and the evolution of the solution of the problem, $\theta(\mathbf{x})$, in the direction $\mathbf{n}$ is undefined. In order to overcome the extra singularity problems associated to this fact in numerical simulation settings, the conductivity tensor (39) can be modified as follows:

$$\mathbb{K}_\epsilon = \mathbf{T} \otimes \mathbf{T} + \epsilon \mathbf{1}, \tag{40}$$

where $\mathbf{1}$ is the unit tensor and ϵ is an isotropic algorithmic conductivity, small enough to fulfill, for practical purposes, Eq. (38) but sufficiently large to break down the singularity of $\mathbb{K}$.

4.3.1. Finite element formulation

Given a finite element discretization of Ω, with n_{elem} elements and n_{node} nodes the discrete counterpart of the continuum problem (37) follows from standard procedures [35]. It can be summarized as follows:

Find

$$\begin{aligned} &\theta^h(\mathbf{x}) = \sum_{i=1}^{i=n_{\text{node}}} N_i \theta_i = [\mathbf{N}]^{\mathrm{T}} \cdot [\boldsymbol{\theta}]; \quad \theta_i|_{\partial_\theta \Omega} = \theta^*, \\ &\begin{cases} [\mathbf{N}] := [N_1, \ldots, N_{n_{\text{node}}}]^{\mathrm{T}}, \\ [\boldsymbol{\theta}] := [\boldsymbol{\theta}_1, \ldots, \boldsymbol{\theta}_{n_{\text{node}}}]^{\mathrm{T}} \end{cases} \end{aligned} \tag{41}$$

such that

$$\begin{aligned} &\mathbf{K} \cdot \boldsymbol{\theta} = \mathbf{0}, \\ &\theta_i|_{\partial_\theta \Omega} = \theta^*, \\ &\mathbf{K} = \int_\Omega [\nabla \mathbf{N}]^{\mathrm{T}} [\mathbb{K}_\epsilon] [\nabla \mathbf{N}] \, \mathrm{d}\Omega, \end{aligned} \tag{42}$$

where $N_i(\mathbf{x})$ are the standard shape functions and $\mathbf{K}$ is the resulting stiffness matrix. Eq. (42) define a linear thermal problem that has to be solved at the beginning of every time step of the original mechanical problem, this providing the required position of the discontinuity paths inside the finite element mesh according to the algorithm in Eq. (32).

If there is no prescribed temperature ($\partial_\theta \Omega = \emptyset \Rightarrow \partial_q \Omega = \partial\Omega$) then the rank of $\mathbf{K}$ is $n_{\text{node}} - 1$. Thus, the temperature has to be prescribed at, at least, one node in order to provide a unique solution of system (42). In addition, in order to preclude solutions of the type $\theta =$ constant (which would not distinguish the different isothermal lines) the temperature should be prescribed at one additional node. The values of the prescribed temperatures are irrelevant for the goal of the model whenever they are not imposed on two points of the same isothermal line.

[10] For numerical simulation purposes, such ill-posedness has only been found for very specific finite element meshes with sides oriented along the isothermal lines. For general meshes, it appears some little numerical extra-conductivity enough to break the ill-posedness.

4.3.2. Generalization to 3D cases

Generalization, from the 2D case considered above, to the general 3D case follows trivially. Let $\mathbf{n}(\mathbf{x})$ be a family of unit vectors, defined at every point in the domain Ω, determining the direction normal to the plane of propagation of the discontinuity. Then, let **S(x)** and **T(x)** be any couple of unit vectors orthogonal to **n** so that

$$\mathbf{S}\cdot\mathbf{n}=\mathbf{T}\cdot\mathbf{n}=0, \tag{43}$$

thus defining the plane (tangent to them) of propagation of the discontinuity. The family of surfaces (*tracking surfaces*), enveloping both vectors, **S** and **T**, can be described by a scalar (temperature-like) function $\theta(\mathbf{x})$ such that the isothermal surfaces

$$S_i := \{\mathbf{x}\in\Omega;\ \theta(\mathbf{x})=\theta_{S_i}\} \tag{44}$$

for all the meaningful values of θ_{S_i} are tangent at each point $\mathbf{x}\in\Omega$ to vectors **S** and **T**. Therefore

$$\left.\begin{aligned}\mathbf{S}\cdot\nabla\theta=\nabla\theta\cdot\mathbf{S}=\frac{\partial\theta}{\partial S}=0\\ \mathbf{T}\cdot\nabla\theta=\nabla\theta\cdot\mathbf{T}=\frac{\partial\theta}{\partial T}=0\end{aligned}\right\}\quad\text{in }\Omega, \tag{45}$$

Solutions of problem (45) are also solutions of the following stationary heat conduction problem:

Find: $\theta(\mathbf{x})$ satisfying:

$$\nabla\cdot\mathbf{q}=0 \quad\text{in }\Omega, \tag{46a}$$

$$\mathbf{q}=-\mathbb{K}\cdot\nabla\boldsymbol{\theta}=-\mathbf{S}\frac{\partial\theta}{\partial S}-\mathbf{T}\frac{\partial\theta}{\partial T} \quad\text{in }\Omega, \tag{46b}$$

$$\mathbf{q}\cdot\boldsymbol{v}=(\boldsymbol{v}\cdot\mathbf{S})\frac{\partial\theta}{\partial S}=+(\boldsymbol{v}\cdot\mathbf{T})\frac{\partial\theta}{\partial T}=0 \quad\text{on }\partial_q\Omega, \tag{46c}$$

$$\theta=\theta^* \quad\text{on }\partial_\theta\Omega, \tag{46d}$$

where the anisotropic conductivity tensor $\mathbb{K}$ is given by

$$\mathbb{K}(\mathbf{S}(\mathbf{x}),\mathbf{T}(\mathbf{x}))=\mathbf{S}\otimes\mathbf{S}+\mathbf{T}\otimes\mathbf{T}. \tag{47}$$

The finite element discretization of problem (46) follows the steps of Section 4.3.1 and the temperatures have to be prescribed at, at least, two points to obtain meaningful solutions. Once the temperature field $\theta(\mathbf{x})$ is determined at every node of the finite element mesh, a local (at elemental level) algorithm, the straightforward extension of the one in Eq. (32) to 3D cases, allows one to determine the exact position of the discontinuity surface inside every element.

4.3.3. 3D representative simulation

Now the algorithm is applied to the case of a normal field $\mathbf{n}(\mathbf{x})$ oriented in the radial direction of a cube (see Fig. 11) with the origin at vertex O. That normal field is then

$$\begin{aligned}&\mathbf{n}(\mathbf{x})=\frac{\mathbf{x}}{|\mathbf{x}|},\\ &[\mathbf{n}(\mathbf{x})]=[n_x,n_y,n_z]^{\mathrm{T}}\end{aligned} \tag{48}$$

from which a couple of tangent vectors, **S** and **T**, can be immediately extracted as

$$\begin{aligned}&\mathbf{S}(\mathbf{x})=[0,n_z,-n_y]^{\mathrm{T}},\\ &[\mathbf{T}(\mathbf{x})]=[n_z,0,-n_x]^{\mathrm{T}}.\end{aligned} \tag{49}$$

In Fig. 11(a) the considered finite element mesh, consisting of 1489 tetrahedra, is presented and in Fig. 11(b) the isothermal surfaces are plotted together with the prescribed temperatures. Notice that, as expected, the envelopes are spherical surfaces centered at vertex O.

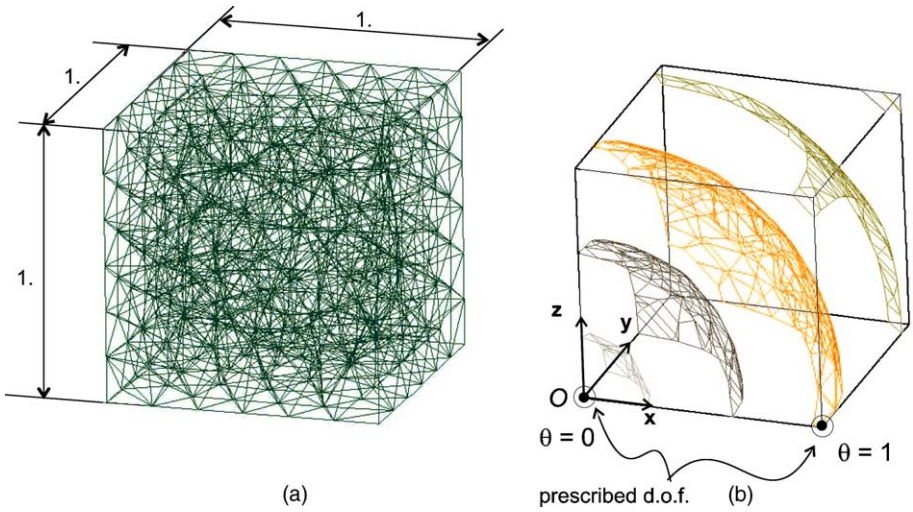

Fig. 11. 3D envelopes of a spherical vector field.

5. Numerical simulation of fracture problems

The approach presented so far is now applied to the numerical simulation of the material failure due to the appearance of multiple strong discontinuities. For those purposes the following ingredients have been considered:

- Finite elements with embedded discontinuities with elemental enrichment. The non-symmetric formulation described in [22] which has proven to be very efficient, is used for all the simulations.
- The isotropic continuum damage model presented in [10] is employed in all the examples. In order to associate failure (and, thus, fracture) to tension stress states (as it is common for quasibrittle materials like concrete) the original iso-tension/compression failure model is slightly modified, to become an *only tension damage model*, in the following sense: the positive (tension) part of the stress tensor is defined as

$$\boldsymbol{\sigma}^{+} := \sum_{i=1}^{3} \langle \sigma_i \rangle \mathbf{p}_i \otimes \mathbf{p}_i, \tag{50}$$

where $\langle \bullet \rangle$ stands for the Macaulay brackets, σ_i for the principal stresses, and $\mathbf{p}_i$ for the principal stress directions. Then, the uniaxial equivalent stress in Eq. (1f) is defined as

$$\phi(\boldsymbol{\sigma}) := \sqrt{E(\boldsymbol{\sigma}^{+} : \mathbf{C}^{-1} : \boldsymbol{\sigma})}, \tag{51}$$

where E is the Young's modulus and $\mathbf{C}$ the usual elasticity tensor.

5.1. Four-points bending test with two notches

The four-points bending test shown in Fig. 12, on a concrete specimen, has been analyzed by using plane stress conditions.

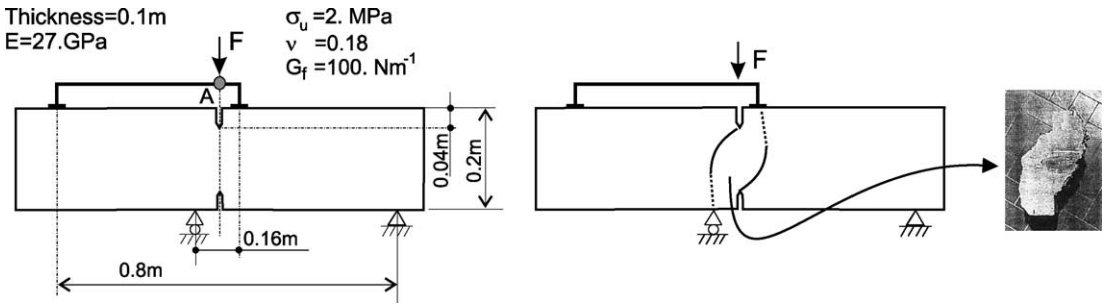

Fig. 12. Four-point bending test for a double-notched beam (from Bocca et al. 1991).

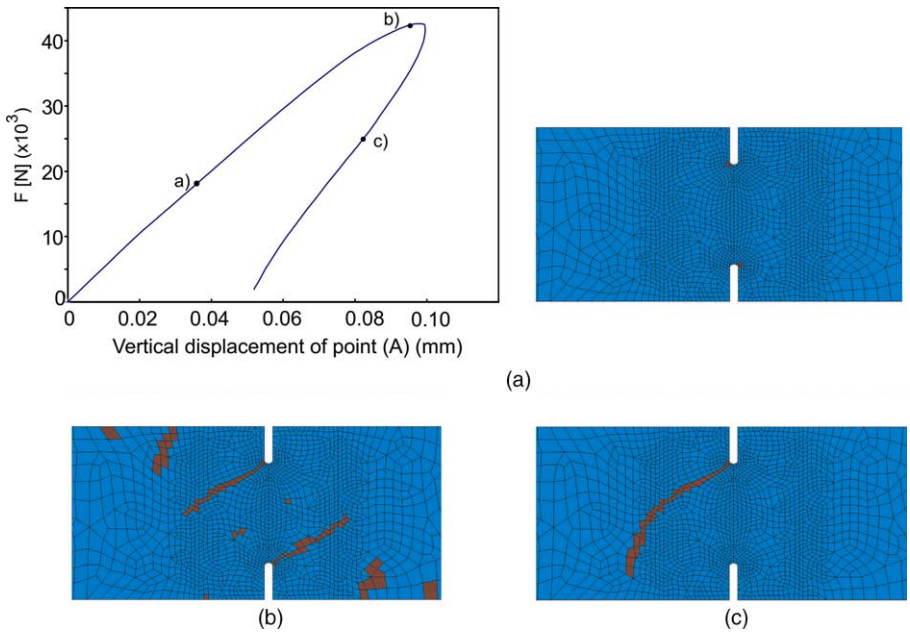

Fig. 13. Four-point bending test for a double-notched beam. Load/displacement curve, and evolution of the active cracks at the center of the specimen.

The experiment corresponds to one of the tests carried out by Bocca et al. [5], who observed that the structure collapsed due to the formation of two primary cracks as displayed in Fig. 12.

Fig. 13 shows the load/displacement curve obtained in the numerical simulation together with the active (opening) crack pattern at the central part of the specimen at different stages of the analysis (marked as (a), (b) and (c) on the load/displacement curve). Before the critical (peak) load (stages (a) and (b)), in addition to several minor (secondary) cracks, two primary symmetric cracks are observed to propagate from the notches matching the experimental cracks. After the peak, load stage (c), only one of the primary cracks remains active while the other arrests.

In order to illustrate the role of the global tracking algorithm of Section 4.2, in Fig. 14 the final crack pattern and the corresponding envelopes of the propagation vector field are presented. There, it can be

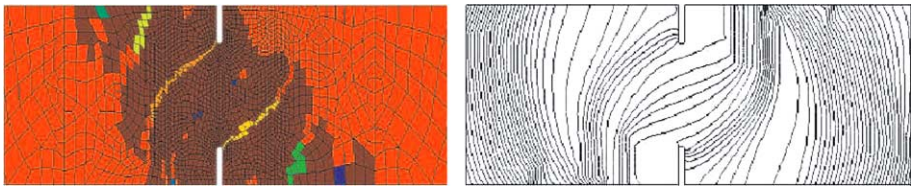

Fig. 14. Four-point bending test for a double-notched beam: (left) crack pattern and (right) isothermal lines.

observed as all the developed cracks are segments of the isothermal lines provided by the heat conduction tracking algorithm.

5.2. Rectangular plate with two geometrical imperfections

This is a theoretical test illustrating the ability of the proposed methodology to capture complex failure mechanisms involving multiple discontinuities interacting with each other. A similar test was done in [8] using a viscoplastic model and a remeshing technology to capture strain localization.

The dimensions of the specimen, the boundary conditions and the considered finite element mesh are shown in Fig. 15. The plane strain case was considered with the following material properties: $E = 3 \times 10^6$ Pa, $\sigma_u = 1 \times 10^3$ Pa, $v = 0.3$, $G_f = 0.01$ N/m. The very low, artificial, value considered for the fracture energy G_f induces a particular structural response which, in addition to the classical limit point, also exhibits several turning points that translate into sudden changes in the deformation and failure modes.

In Fig. 16 the global response curve (horizontal σ_{xx} vs. displacement δ), corresponding to the point A in Fig. 15, is presented together with the evolution of the active (opening) cracks for different stages of the analysis. At the initial stages (a) and (b) a failure mode, characterized by four cracks initiating at both openings, develops. After the peak load, and coinciding with the first snap back, a sudden change of failure mode takes place (stages (c), (d), and (e)) and the cracks at the right-hand side opening arrest. The second turning point develops those cracks emerging from the left-hand side opening (stage (f)). In stages (g) and (h), at the third turning point, a new change of failure mode results into arresting the lower of those cracks and fully developing the upper one.

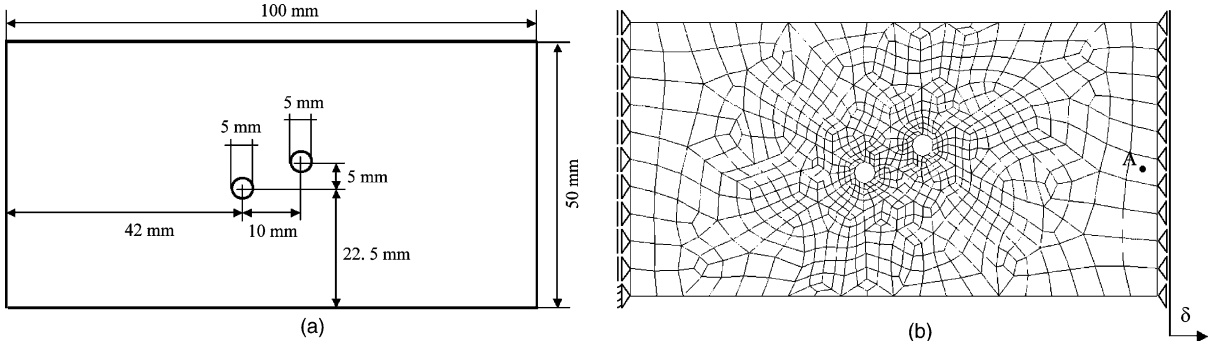

Fig. 15. Rectangular plate with two openings. Geometry and finite element mesh.

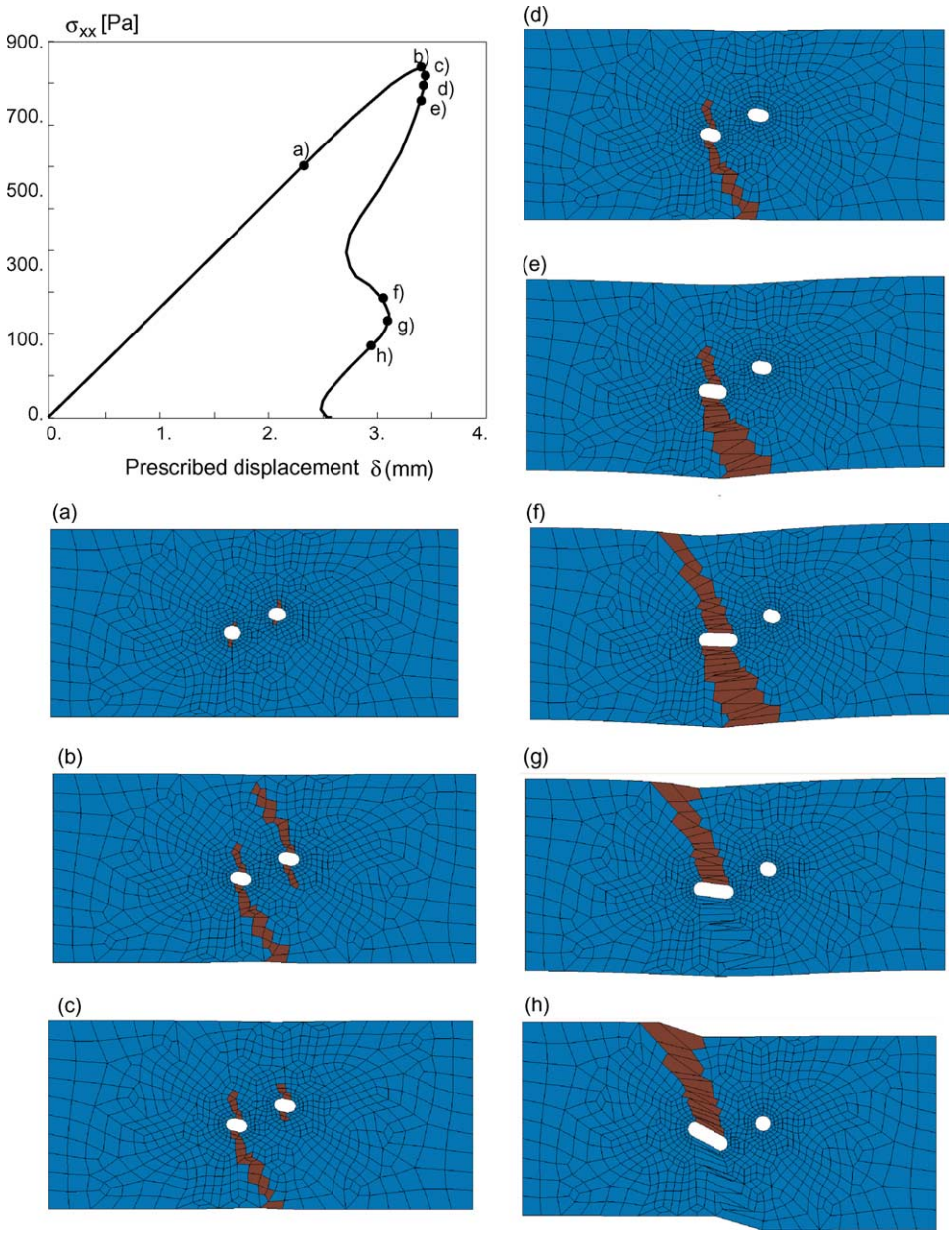

Fig. 16. Rectangular plate with two openings. σ_{xx}-imposed displacement curve and active fracture pattern for different stages of the deformation process.

6. Concluding remarks

The final goal of failure mechanics is to consider the structural failure as a unique physical fact, independently of the variety of causes responsible for the collapse. In this sense, local and global failure (from material and geometrical non-linearities) should be, in many cases, considered together in a coupled

manner. Since the natural format for the geometrical failure (geometrical instability and buckling) is continuum, it appears that a material failure approach also set in this continuum format would be preferable to combine both types of failure. Besides, one could find additional advantages in continuum material failure tools for identification of material properties from the "smeared" data obtained in laboratory tests. Furthermore, implementation of continuum material failure models in existing non-linear analysis codes appears easier and more natural than the discrete ones.

This work has intended to step in this direction. Throughout this paper a continuum approach to material failure in a strong discontinuity setting has been presented. Its main feature is that a continuum format is kept in both the continuum bulk and the discontinuity interface of the material. The activation, via a chosen local failure criterion, of the strong discontinuity kinematics at the discontinuity interfaces induces the fulfillment of a discrete traction–separation law, which turns out to be a projection of the continuum dissipative constitutive model onto the discontinuity interface, and connects the approach with the discrete failure mechanics. However this separation law is never explicitly derived nor implemented in the simulation code, but inherited from the particular family of continuum models that is considered in the continuum format. In that sense the approach is completely general and can be applied to any continuum constitutive model. Moreover, although only infinitesimal strain kinematics has been considered here, its extension to finite strains can also be done in a very similar manner [24].

As for numerical aspects, the approach can be inserted in any spatial discretization scheme, and, in particular, it can take advantage of the recent developments in terms of finite elements with embedded discontinuities to capture displacement jumps. In this context, the classic drawbacks of lack of mesh size and mesh bias objectivity can be totally removed. On the other side, and since the discontinuities are embedded in finite elements, there is no intrinsic limitation in terms of the maximum size of the finite element mesh, the computational cost can be kept moderate and even remeshing is not intrinsically necessary.

However, and as in more traditional methods, the computational treatment, in terms of the discontinuity path tracking, can become cumbersome if classical propagation algorithms, that work very well for a single discontinuity, are intended to be extended to the multiple fractures case. Also the extension of one single crack model to 3D cases presents many difficulties.

In this work an alternative, in terms of a global tracking algorithm has been presented. The idea is to perform an additional computation at every time step of the analysis to determine, at once, all the candidates to be discontinuity paths. Then, with this information in hand, selecting the real ones becomes an easier task. The presented heat conduction-like algorithm to compute the envelopes of the propagation vector field, is simple (it involves very well known physical concepts), computationally efficient (it implies a linear analysis with one degree of freedom per node, the temperature, on the same mesh than for the mechanical analysis) and it is easy to implement (trivial in a thermo-mechanical code like the one used in this work [6]).

Acknowledgements

Financial support from the Spanish Ministry of Science and Technology, through grant MAT2001-3863-C03-03, and from the Catalan Government Research Department, through the CIRIT grant 2001-SGR 00262, is gratefully acknowledged.

References

[1] F. Armero, K. Garikipati, An analysis of strong discontinuities in multiplicative finite strain plasticity and their relation with the numerical simulation of strain localization in solids, Int. J. Solids Struct. 33 (20–22) (1996) 2863–2885.

[2] Z.P. Bazant, Crack band theory for fracture of concrete, Mater. Construct. (93) (1983) 155–177.
[3] Z.P. Bazant, J. Planas, Fracture and size effect in concrete and other quasibrittle materials, CRC Press, Boca Raton, FL, 1998.
[4] T. Belytschko, N. Moës, S. Usui, C. Parimi, Arbitrary discontinuities in finite elements, Int. J. Numer. Methods Engrg. 50 (2001) 993–1013.
[5] P. Bocca, A. Carpintieri, S. Valente, Size effect in the mixed mode crack propagation: softening and snap-back analysis, Engrg. Fract. Mech. 35 (1990) 159–170.
[6] M. Cervera, C. Agelet de Saracibar, M. Chiumenti, COMET: a multipurpose finite element code for numerical analysis in solid mechanics. Technical Report, Technical University of Catalonia (UPC), 2001.
[7] R. de Borst, L.J. Sluys, H.B. Muhlhaus, J. Pamin, Fundamental issues in finite element analyses of localization of deformation, Engrg. Comput. 10 (1993) 99–121.
[8] P. Diez, M. Arroyo, A. Huerta, Adaptivity based on error estimation for viscoplastic softening materials, Mech. Cohes.-Frict. Mater. 5 (2000) 87–112.
[9] E.N. Dvorkin, A.M. Cuitino, G. Gioia, Finite elements with displacement embedded localization lines insensitive to mesh size and distortions, Int. J. Numer. Meth. Engrg. 30 (1990) 541–564.
[10] R. Faria, J. Oliver, M. Cervera, A strain-based plastic viscous-damage model for massive concrete structures, Int. J. Solids Struct. (14) (1998) 1533–1558.
[11] A. Hillerborg, The theoretical basis of a method to determine the fracture energy gf of concrete, Mater. Construct. 18 (106) (1985) 291–296.
[12] J. Lemaitre, A continuous damage mechanics model for ductile fracture, J. Engrg. Mater. Technol., Trans. ASME 107 (1985) 83–89.
[13] H.R. Lofti, P. Benson Shing, Embedded representation of fracture in concrete with mixed finite elements, Int. J. Numer. Methods Engrg. 38 (1995) 1307–1325.
[14] J. Lubliner, Plasticity Theory, Mcmillan Publishing Company, New York, 1990.
[15] N. Moës, N. Sukumar, B. Moran, Belytschko T. An extended finite element method (X-FEM) for two and three-dimensional crack modelling. In ECCOMAS 2000, Barcelona, Spain, September 11–14, 2000. Vienna University of Technology, Austria, ISBN 3-9501554-0-6.
[16] A. Needleman, V. Tvergard, Analysis of plastic localization in metals, Appl. Mech. Rev. (1992) 3–18.
[17] J. Oliver, Continuum modelling of strong discontinuities in solid mechanics using damage models, Comput. Mech. 17 (l–2) (1995) 49–61.
[18] J. Oliver, Modeling strong discontinuities in solid mechanics via strain softening constitutive equations. Part 2: numerical simulation, Int. J. Numer. Methods Engrg. 39 (21) (1996) 3601–3623.
[19] J. Oliver, On the discrete constitutive models induced by strong discontinuity kinematics and continuum constitutive equations, Int. J. Solids Struct. 37 (2000) 7207–7229.
[20] J. Oliver, M. Cervera, O. Manzoli, Strong discontinuities and continuum plasticity models: the strong discontinuity approach, Int. J. Plast. 15 (3) (1999) 319–351.
[21] J. Oliver, A. Huespe, M.D.G. Pulido, E. Chaves, From continuum mechanics to fracture mechanics: the strong discontinuity approach, Engrg. Fract. Mech. 69 (2) (2002) 113–136.
[22] J. Oliver, A. Huespe, E. Samaniego, A study on finite elements for capturing strong discontinuities, Int. J. Numer. Meth. Engrg. 56 (2003) 2135–2161.
[23] J. Oliver, A.E. Huespe, Theoretical and computational issues in modeling material failure in strong discontinuity scenarios, Comput. Methods Appl. Mech. Engrg., in press.
[24] J. Oliver, A.E. Huespe, M.D.G. Pulido, E. Samaniego, On the strong discontinuity approach in finite deformation settings, Int. J. Numer. Meth. Engrg. 56 (2003) 1051–1082.
[25] J. Oliver, A.E. Huespe, E. Samaniego, E.W.V. Chaves, On strategies for tracking strong discontinuities in computational failure mechanics. In: H.A. Mang, F.G. Rammer-storfer, J. Eberhardsteiner, (Eds.), Proceedings of the Fifth World Congress on Computational Mechanics (WCCM V), Swansea, July 7–12, 2002, Vienna University of Technology, Austria, ISBN 3-9501554-0-6, Available from <http://wccm.tuwien.ac.at>.
[26] J.G. Rots, P. Nauta, G.M.A. Kusters, J. Blaauwendraad, Smeared crack approach and fracture localization in concrete, Heron 30 (l) (1985) l–49.
[27] K. Runesson, N.S. Ottosen, D. Peric, Discontinuous bifurcations of elastic-plastic solutions at plane stress and plane strain, Int. J. Plast. 7 (1991) 99–121.
[28] J. Simo, J. Oliver, A new approach to the analysis and simulation of strong discontinuities, in: Z.P. Bazant et al. (Eds.), Fracture and Damage in Quasi-brittle Structures, E&FN Spon, 1994, pp. 25–39.
[29] J. Simo, J. Oliver, F. Armero, An analysis of strong discontinuities induced by strain-softening in rate-independent inelastic solids, Computat. Mech. 12 (1993) 277–296.
[30] J.C. Simo, T.J.R. Hughes, Computational Inelasticity, Springer, Berlin, 1998.

[31] J.C. Simo, J.W. Ju, Stress and strain based continuum damage models: I formulation, Int. J. Solids Struct. 15 (1987) 821–840.
[32] E. Stein, P. Steinmann, C. Miehe, Instability phenomena in plasticity: modelling and computation, Computat. Mech. 17 (1995) 74–87.
[33] G.N. Wells, L.J. Sluys, A new method for modelling cohesive cracks using finite elements, Int. J. Numer. Methods Engrg. 50 (2001) 2667–2682.
[34] K. Willam, Constitutive models for engineering materials, in: Encyclopedia of Physical Science and Technology, third ed., Academic Press, New York, 2000, pp. 603–633.
[35] O.C. Zienkiewicz, R.L. Taylor, The Finite Element Method, Butterworth-Heinemann, Oxford, UK, 2000.